UC Davis
UC Davis Previously Published Works

Title

A wirelessly programmable, skin-integrated thermo-haptic stimulator system for virtual reality.

Permalink

https://escholarship.org/uc/item/3pc8p7w0

Journal

Proceedings of the National Academy of Sciences, 121(22)

Authors

Kim, Jae-Hwan

Vázquez-Guardado, Abraham

Luan, Haiwen

et al.

Publication Date

2024-05-28

DOI

10.1073/pnas.2404007121

Peer reviewed

A wirelessly programmable, skin-integrated thermo-haptic stimulator system for virtual reality

Jae-Hwan Kim[a,b,1], Abraham Vázquez-Guardado[a,c,1] (ID), Haiwen Luan[d,1], Jin-Tae Kim[e,1], Da Som Yang[a], Haohui Zhang[f], Jan-Kai Chang[a,g] (ID), Seonggwang Yoo[a] (ID), Chanho Park[a], Yuanting Wei[f], Zach Christiansen[a], Seungyeob Kim[h], Raudel Avila[i], Jong Uk Kim[a], Young Joong Lee[a] (ID), Hee-Sup Shin[a] (ID), Mingyu Zhou[a], Sung Woo Jeon[b], Janice Mihyun Baek[j], Yujin Lee[j], So Young Kim[j], Jaeman Lim[k], Minsu Park[l], Hyoyoung Jeong[m] (ID), Sang Min Won[n], Renkun Chen[d], Yonggang Huang[a,f,o] (ID), Yei Hwan Jung[k,2] (ID), Jae-Young Yoo[p,2], and John A. Rogers[a,o,q,r,s,2] (ID)

Contributed by John A. Rogers; received February 26, 2024; accepted April 13, 2024; reviewed by Jun Chen and Firat Güder

Sensations of heat and touch produced by receptors in the skin are of essential importance for perceptions of the physical environment, with a particularly powerful role in interpersonal interactions. Advances in technologies for replicating these sensations in a programmable manner have the potential not only to enhance virtual/augmented reality environments but they also hold promise in medical applications for individuals with amputations or impaired sensory function. Engineering challenges are in achieving interfaces with precise spatial resolution, power-efficient operation, wide dynamic range, and fast temporal responses in both thermal and in physical modulation, with forms that can extend over large regions of the body. This paper introduces a wireless, skin-compatible interface for thermo-haptic modulation designed to address some of these challenges, with the ability to deliver programmable patterns of enhanced vibrational displacement and high-speed thermal stimulation. Experimental and computational investigations quantify the thermal and mechanical efficiency of a vertically stacked design layout in the thermo-haptic stimulators that also supports real-time, closed-loop control mechanisms. The platform is effective in conveying thermal and physical information through the skin, as demonstrated in the control of robotic prosthetics and in interactions with pressure/temperature-sensitive touch displays.

thermo-haptic stimulator

Mechanoreceptors and thermoreceptors exist in distributed configurations throughout the skin across all regions of the body as the receptive components of sensory nerves that serve essential roles in perceiving external stimuli (1–3). Deterioration of these sensory detection mechanisms and/or the associated afferent peripheral nerves can impose debilitating limitations on many aspects of daily life (4, 5). Engineered interfaces that can seamlessly integrate with the skin to engage healthy receptors in a programmable fashion can form the basis of sensory substitution to circumvent such deficiencies, with important potential for patients with impaired sensory nerves, with amputations, or with needs in rehabilitation (6–11). Adapted versions of the same technologies can also be integrated with virtual reality (VR) and augmented reality (AR) interfaces as platforms for enhancing user experiences in gaming, entertainment, and social interactions (12–15).

Recent research activity in this area establishes various options in these types of haptic interfaces, utilizing arrays of mechanical and/or electrical actuators with a focus not only on the fingertips, a traditional emphasis, but across large areas of the body (12, 14, 16–20). Additional examples are in electrothermal systems that use resistive heaters or thermoelectric pellets (21–23). Combined technologies of these types have potential as spatiotemporal thermo-haptic interfaces, including those in large, flexible forms compatible with the skin. While recently reported devices can enhance VR/AR systems by simulating realistic perceptions through coordinated mechanical and thermal stimulation, challenges remain in achieving adequate spatial resolution, power efficiency, stimulation strength, and dynamic response speed. Notable examples produce multiple sensations with mechanical, electrotactile, and thermal inputs, although in a spatially separated manner with temporal responses and control schemes that may not satisfy certain practical requirements (12). In all cases, the desired capabilities must be achieved in lightweight, thin interfaces that can comfortably mount on the skin.

This paper introduces a wireless, skin-compatible thermo-haptic technology that combines arrays of thermal and haptic stimulators in spatially integrated, vertically coupled configurations to enable delivery of programmable patterns of enhanced vibrational displacement and high-speed thermal stimulation across the entire body, with low latency control mechanisms. Experimental measurements and computational studies capture the fundamental

Significance

Artificially programmed sensory stimulation of the skin can complement audio and video inputs for advanced virtual and augmented reality systems. Engineering challenges are in realizing wearable technologies that can produce desired patterns of actuation across large areas of the skin in a wirelessly coordinated manner. Here, we present a skin-compatible interface of this type, designed to activate thermal and mechanical receptors in the skin, with fast and accurate control schemes, applicable to large area regions of the body. This advance not only enhances the realism of sensory experiences in virtual reality environments but it also enables a broad range of additional possibilities in entertainment, social interactions, medical interventions, and rehabilitation strategies.

[1]J.-H.K., A.V.-G., H.L., and J.-T.K. contributed equally to this work.

[2]To whom correspondence may be addressed. Email: yjung@hanyang.ac.kr, jy.yoo@skku.edu, or jrogers@northwestern.edu.

operating mechanisms and various capabilities in enhanced perception efficiency. Implementations in real-time closed-loop feedback schemes serve as the basis of examples of use with robotic prosthetic hands and pressure/temperature-sensitive touch displays.

Results

Overall Design. The thermo-haptic stimulator system exploits thin, flexible materials, structural designs, and soft elastomers to join hard, rigid components in mechanically optimized layouts that can create dynamic spatiotemporal patterns of stimulation to the skin. The resulting platforms can mount on nearly any location of the body over large areas, Fig. 1A The approaches follow design rules for soft, hybrid electronics, in a wireless system that exploits Bluetooth low energy (BLE) communication protocols, as shown in an exploded view schematic illustration in Fig. 1B. This example includes an array of 15 individually addressable thermo-haptic stimulators arranged with a 19 mm center-to-center separation, consistent with two-point discrimination thresholds for perception in regions of the body such as the back, chest, legs, and arms (9). Each stimulator includes a miniaturized eccentric rotating mass (ERM, 7 mm diameter) vibromechanical actuator bonded on top of a small-scale thermoelectric cell (TE cell, $6 \times 6 \times 2.7$ mm^3) (Fig. 1C). This geometry provides the basis for delivering high-resolution (1 thermo-haptic unit per 2.3 cm^2) patterns of thermo-haptic stimulation to the skin, as described in detail in the following (Fig. 2 A–C and *SI Appendix,* Table S1).

Principles of Mechanical Stimulation. The ERM actuator rotates a counterweight or eccentric mass upon activation with a direct-current (d.c.) voltage, such that induced unbalanced forces lead to vibrations primarily parallel to the skin surface (16). Operation occurs at frequencies in the 50 to 150 Hz range, aligned with the sensitivity of Pacinian corpuscles in the skin (24). The stacked geometry of the ERM actuator on the TE cell increases the height of the center of mass of the former relative to the surface of the skin, by approximately 3 mm (*SI Appendix,* Fig. S1). This increase reduces the natural frequency for operation at 3.3 V from 134 Hz to 101 Hz (*SI Appendix,* Fig. S2). and increases the amplitude of the vibration from 73 μm to 160 μm (Fig. 2F). This increased

amplitude not only stimulates the glabrous skin, which has a low vibrotactile detection threshold of several tens of nanometers, but also the hairy skin, which is relatively insensitive and requires displacements of more than ~100 μm (25, 26).

Quantitative studies utilizing particle tracking velocimetry (PTV) and three-dimensional digital image correlation (3D-DIC) (27), together with simple mechanics models of the dynamics, capture the physics. PTV tracks the center of oscillation (Fig. 2 D and E) and 3D-DIC yields spatiotemporal maps of deformations in an underlying skin phantom (*SI Appendix,* Fig. S3). Fig. 2D and *SI Appendix,* Fig. S2 A and B, present schematic illustrations and photographs of an experimental setup with bilayer phantoms, ERM actuators, and intermediate structures that share the same diameters as the actuators with heights, h, in the range of 0 to 9 mm to simulate the effects of the TE cell. Fig. 2E shows the lateral displacements (Δx) at the center of an actuator as a function of h. As h increases, the amplitude increases, and frequency decreases (Fig. 2F and *SI Appendix,* Fig. S2C and Movie S1). *SI Appendix,* Fig. S3, summarizes radial displacement contours at representative times for three values of h. Increasing h enhances momentum transfer to the tip, resulting in concentrated mechanical stimulation with increased amplitude at this region. These trends are consistent with the response of a simple forced damped oscillator with a spring constant of the combined ERM actuator and intermediate structure. Additional details are in *Methods*. Related findings follow from finite-element analysis (FEA) of as a function of h and phantom skin modulus E_{skin} as shown in *SI Appendix,* Fig. S4. Additional experimental studies indicate that operating the ERM above a duty cycle of 40% stabilizes the vibration, as a simple harmonic motion with a single sinusoidal form (*SI Appendix,* Fig. S5A). As expected, tests confirm that these motions do not depend on temperature across a physiologically relevant range (*SI Appendix,* Fig. S5B).

Principles of Thermal Stimulation. The Peltier effect in the TE cells produces temperature differences between the top and bottom sides upon application of an electrical current. As such, the direction and magnitude of the current determine the direction of heat flow and thus the amount of heat transferred to the skin surface. This process activates the hot or cold receptors in the skin to a
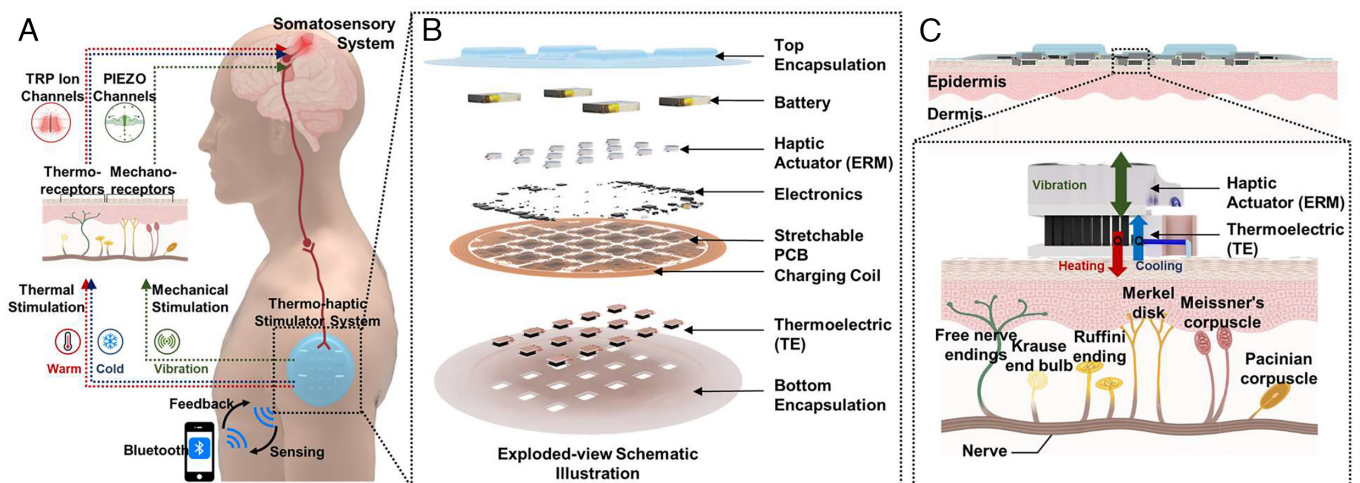

Fig. 1. Design and operation of a wireless thermo-haptic stimulator system. (A) Illustration of the overall operation and the perception process. A user receives three different stimuli (vibration, heating, and cooling) through receptors in the skin, subsequently processed by the brain. (B) Exploded view schematic illustration of the batteries, haptic actuators, electronic components, thermal stimulator, temperature sensors, and encapsulation layers. (C) Illustration of the device on the skin and corresponding skin sensory receptors: free nerve endings (pain, heat, cold), Krause end bulb (touch, cold), Ruffini ending (pressure, heat), Merkel disk (touch), Meissner's corpuscle (touch), and Pacinian corpuscle (pressure). Thermoelectric (TE) cells induce thermal perceptions via heating or cooling, thereby stimulating the thermal receptors. Haptic actuators (ERM) generate vibrations, thus stimulating the mechanoreceptors.
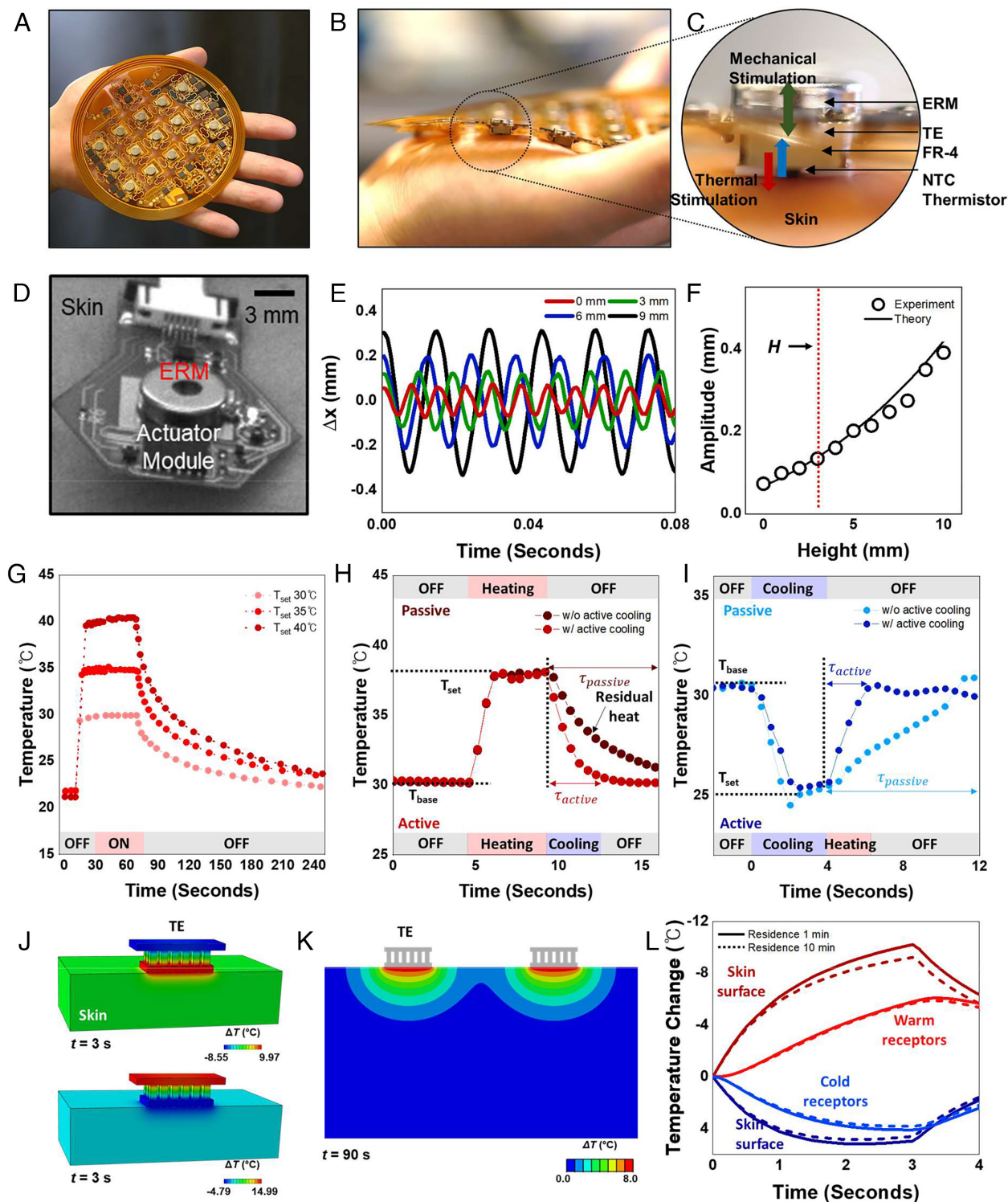
Fig. 2. Operating principles, mechanical and thermal characteristics of the thermo-haptic stimulators. (*A*) Photograph of a complete system resting on a hand. (*B*) Angled side view photograph that highlights an individual thermo-haptic stimulator. (*C*) A magnified view of the stimulator illustrating the mechanical (green) and thermal (blue and red) mechanisms for stimulating the skin. (*D*) Photograph of an ERM actuator during particle tracking velocimetry (PTV) measurements. (*E*) In-plane displacement, Δ*x*, as a function of time measured at the center of a thermo-haptic stimulator with different values of *h*. (*F*) Amplitude as a function of *h*, (*G*) Representative PID-controlled temperature profile for thermal stimulation. (*H*) Comparison of normal operation and reverse current operation (active cooling) to accelerate the return to baseline temperature after heating. (*I*) Comparison of normal operation and reverse current operation (active heating) to accelerate the return to baseline temperature after cooling. (*J*) Finite-element analysis of the temperature distribution of the skin and the thermoelectric module after 3 s of heating (*Top*) and cooling (*Bottom*). (*K*) Finite-element analysis of temperature responses at the skin surface and the locations of thermoreceptors for operation with residence times of 1 and 10 min. (*L*) Finite-element analysis of skin temperature responses associated with operation of two adjacent thermoelectric modules with a center-to-center distance of 19 mm.

corresponding degree. A thermistor attached to the surface of the TE cell that contacts the skin captures the local temperature in real time (*SI Appendix*, Fig. S6*A*). A circuit board serves as a three-dimensional electrical interconnect for the thermistor, allowing for direct contact with the skin by matching the height of the TE cell (*SI Appendix*, Fig. S6*B*). Measurements of temperature provide feedback for a

closed-loop PID controller (*SI Appendix*, Fig. S7) designed to reach and hold to a set temperature across a range of 35 to 50 °C to within ~0.1 °C, as described in detail subsequently (*SI Appendix*, Fig. S8). Fig. 2 *H* and *I* summarize measurement results that exploit this PID control with and without active cooling and heating after a period of increased or decreased temperature, respectively. For both heating and cooling cases, simulations match the measurements. In the example of Fig. 2*H*, a current of 0.4 A raises the temperature to a value close to the set point, after which a current of 0.22 A maintains the temperature. For passive cooling, heat diffuses to the environment or through the skin into the body. For active cooling, a reversed current induces a flux of heat from the bottom of the TE cell to the top, thereby accelerating the return of the temperature to the initial value (*SI Appendix*, Fig. S9). In Fig. 2*I*, similarly, a current of 0.4 A reduces the temperature to a set point, after which a current of 0.17 A maintains this temperature. In the stacked geometry of the thermo-haptic stimulator, the ERM actuator serves as a heatsink to reduce the temperature difference between the top and bottom of the TE cell, thereby increasing the TE heating/cooling power efficiency (*SI Appendix*, Figs. S10 and S11 *A–D*). During passive heat dissipation, the ERM actuator enhances the surface area to improve thermal coupling to the environment (*SI Appendix*, Fig. S11 *E–G*).

Spatiotemporal Characteristics of Heating for Thermal Perception. Thermal receptors in the skin respond most sensitively to rapid changes in temperature. High-fidelity thermal stimulation thus depends on the ability of the TE cell to induce fast dynamic changes in the temperature of the skin, at depths that correspond to the locations of the thermoreceptors. For thermal perception at the natural temperature of the skin (30 to 32 °C), an increase of at least 0.5 °C can produce a warming sensation provided that the heating rate is at least 0.1 °C/s (28). Similarly, a decrease of at least –0.3 °C can produce a cooling sensation at a cooling rate of at least –0.1 °C/s. The minimum times required to reach temperature differences of 0.5 °C and –0.3 °C with the stimulators reported here are 89 ms and 132 ms, respectively, corresponding to respective heating and cooling rates of 5.6 °C/s and –2.3 °C/s.

Due to sensory adaptation, additional thermal sensations require increased changes in temperature. For example, for skin adapted to a temperature of 36 °C, a warming sensation requires a temperature change of at least 0.5 °C, but a cooling sensation requires a change of at least –1.8 °C (29). The time required to produce this minimal warming sensation is 117 ms, corresponding to a rate of 4.3 °C/s; for cooling the time and rate are 443 ms and –1.8 °C/s, respectively. Similarly, for skin adapted to 26 °C, the threshold for a warming sensation increases to 2.0 °C (29), which can be reached within 634 ms, corresponding to a heating rate of 3.2 °C/s. Overall, the thermo-haptic stimulators reported here can provide warming/cooling sensations for natural skin temperatures within 634 ms.

Another important consideration is that thermal perception follows from the activity of cold and warm receptors that reside at depths 150 to 200 μm and 300 to 500 μm below the surface of the skin, respectively (30). The thermal resistance and thermal capacitance of the skin cause a slight delay before changes in the temperature of the surface of a TE cell reach the thermal receptors. Dynamic FEA of these features in thermal transport reveals the essential effects (Fig. 2*J*). Specifically, the times required for temperature at the surface of the skin to increase by 1, 2, 3, and 4 °C are 0.12, 0.28, 0.38, and 0.57 s, respectively; corresponding times for the warm receptors are 0.70, 1.05, 1.25, 1.48, and 1.92 s. Under the same conditions, the times required to reduce the skin surface temperature by 1, 2, and 3 °C are 0.15, 0.33, and

0.55 s, respectively, and those of the cold receptors are 0.43, 0.80, and 1.30 s. The times to reach the cold receptors (150 μm depth) are thus 2.34 times larger than those for the surface of the skin. This factor is 3.69 for warm receptors (500 μm depth). In all cases, the delay times are less than 0.7 s for changes in temperatures of the thermoreceptors by 1 °C (*SI Appendix*, Fig. S12*A*). The ratios between temperatures at the surface and at certain depths appear in *SI Appendix*, Fig. S12*B*.

Additional thermal transport effects follow from diffusion parallel to the surface of the skin, with the potential to activate thermal receptors at adjacent locations. FEA results in Fig. 2*K* show temperature profiles associated with operation of neighboring stimulators with a center-to-center distance of 19 mm. When these stimulators heat the skin to 40 °C for 180 s, the temperature of the skin between the cells increases by 0.7 °C, respectively, at depths as large as 2 mm (*SI Appendix*, Fig. S12*C*). These effects thus influence not only the timescales and the depths associated with these thermal processes, but they also set limits on the lateral resolution.

All of these results rely on the simplifying assumption that the thermal conductivity of the skin does not depend on temperature. Living systems, however, respond actively to changes in the temperature. For the case of skin, these responses include constriction or dilation of the blood vessels. These changes affect the effective thermal conductivity and they can also alter the base temperature of the skin. Experimental studies of these responses follow measurement methods described previously (*SI Appendix*, Fig. S13) (31). The focus is on the thermal conductivity of the skin following heating across different areas (diameters of 4.5 and 18 mm), for various changes in temperature (32, 36, and 40 °C) and timescales (1, 3, 5, and 10 min). The results show increases in the conductivity with increasing areas, temperatures, and times, likely due to corresponding increases in induced vasodilation (*SI Appendix*, Fig. S14) (32, 33). The maximum changes for the conditions explored here for local (4.5 mm) heating are ~20% (native thermal conductivity: 0.46 W/m·K, maximum thermal conductivity: 0.58 W/m·K for 40 °C and 10 min, 15.9 mm², back of a hand). For global (18 mm) heating the changes can exceed 50% (native thermal conductivity: 0.43 W/m·K, maximum thermal conductivity: 0.67 W/m·K for 40 °C and 10 min, 254.5 mm², back of a hand).

Such temperature-dependent effects can be explicitly included in simulations. For example, Fig. 2*L* shows the temperature-time profiles of at the skin surface and at depths characteristic of those associated with hot and cold receptors. The temperature-time profiles were calculated during heating/cooling with a TE cell over durations of 1 and 10 min. The dynamics for these two cases are similar, thereby suggesting that the effects of temperature-dependent thermal conductivity of the skin can be neglected for practical uses contemplated in the following (Fig. 2*L*).

Another consideration is that in applications, the time dependence of the change in temperature imposed onto the skin to represent contact with an object in a virtual environment depends not only on the temperature of that object but also its thermal conductivity (34). *SI Appendix*, Fig. S15, shows the simulated and measured temperature profiles of the skin when contacted to objects with different thermal conductivities [tungsten: 40 to 50 W/m·K (35), steel: 21 W/m·K (36), ceramic: 7.5 W/m·K (37)] at a temperature of 45 °C. As also illustrated in *SI Appendix*, Fig. S15, the stimulators described here can reproduce sensations relevant to materials with a range of thermal conductivities.

Wireless, Skin-Integrated System for Thermo-Haptic Modulation. A double-sided flexible printed circuit board (fPCB, 110 μm thick) cut into an open network geometry supports necessary electronic

components, hybrid unit arrays, associated control circuits, a wireless BLE communication module, four lithium-ion polymer batteries (70 mAh), and a 6-turn single sided inductive coil that surrounds the perimeter (109 mm diameter) for wireless battery charging at a frequency of 13.56 MHz (Fig. 2*A*). A soft encapsulating elastomer isolates all regions except for the surfaces of the thermo-haptic stimulators in contact with the skin (Fig. 2*C* and *SI Appendix*, Fig. S16). Each island within the fPCB includes one thermo-haptic stimulator, with physical and electrical interconnects to adjacent islands in stretchable, serpentine geometries for the distribution of power, control, or data acquisition across the array. The center edge of each island includes a notch to extend the length of the corresponding serpentine interconnects, for improved mechanical compliance (*SI Appendix*, Fig. S17). FEA results for the mechanics of the system with optimized choices in layout appear in Fig. 3*A* for various deformations such as stretching, bending, twisting, and pressing against a spherical surface. Corresponding optical images of a completed device are in Fig. 3*B*. These examples, which are representative of those associated with mounting the interface on different large regions of anatomy of an adult, induce strains across the copper and polyimide layers of the fPCB that remain below the material failure thresholds (PI elongation at break ~7.4%, Cu elongation at break ~58%) (*SI Appendix*, Figs. S18 and S19). Specifically, the peak strains in the copper layers for these cases of bending, twisting, and pressing are 0.5%, 0.4%, and 0.8%, and the peak strains in the polyimide are 0.8%, 3.1%, and 3.1%, respectively. The results ensure comfortable interfaces to the skin, supported by a thin, double-sided medical-grade silicone adhesive (2477P, 3 M) as shown on the back, arms, calves, and thighs in Fig. 3*C*. The total production cost for a thermo-haptic stimulator system of the type reported here, including the ~500 constituent components, is in the range of $200, depending strongly on volumes and specific manufacturing methods (*SI Appendix*, Table S2).

Circuit Designs and Operating Principles. As described previously, the devices comprise subsystems strategically distributed across the fPCB to provide wireless BLE communication, control, power management, logic, and analog interfaces, along with sensors and actuators to achieve the overall functionality and performance. Fig. 3*D* presents circuit and block diagrams. This example supports 15 independent thermo-haptic stimulators, with 15 associated digital signals for heating control, 15 for cooling control, and 15 for haptic control. In addition, 15 analog to digital converter (ADC) units capture the temperature at each stimulator. The electronic control relies on an Arm Cortex M3 CPU that operates at 24 MHz and supports Bluetooth low energy (BLE) 5.1 radio frequency (RF) communication. Although the CPU has limited general input/output (GPIO) and analog input ports, it interfaces with three peripheral digital input/output port expanders (16-GPIOs each) and one ADC chip (12 input channels) via I2C at 400 kHz to satisfy the control and sensing demands. When combined with wireless bidirectional communication to an iOS device, the hardware configuration and custom firmware can deliver programmable patterns of haptic or thermal stimulation to the skin on a real-time basis, with latency in the range of 30 ms as given by the BLE connection interval.

The sensitivity to mechanical and thermal stimulation varies from individual to individual and from one skin area to another, due to different distributions of mechanical and thermal receptors. Therefore, control algorithms that can generate personalized stimulation patterns tailored to each individual case are essential. A dedicated graphic user interface (GUI) allows for interactions

through encoded patterns of actuation, updated at rates of 30 ms, to control the spatial and temporal dynamics of operation. Within each Bluetooth transaction, the system receives a 16-byte configuration vector that contains information for stimulator configuration. For example, the header of this vector indicates the modality (haptic or thermal), and the subsequent 15 bytes encode the values of operation for the selected modality, i.e., pulse width for haptic or set temperature for thermal actuation.

A pulse width modulation (PWM) scheme based on three digital signals controls the operation of each thermo-haptic stimulator, independently. Specifically, a PWM signal at 10 Hz drives the operation of the haptic actuator, and its sentinel indicator, using an n-channel MOSFET power stage. Wirelessly defined pulse widths (1 to 99 ms) determine the amplitude of vibrotactile actuation by controlling effective power delivered to each ERM (20). The other two PWM signals drive a bidirectional H-bridge power stage to control the polarity of the current flowing through the TE cell and, at the same time, to enable the current limiting integrated circuit (IC) via a two input OR logic gate as the basis to manage power during the idle states. The pulse width of the PWM signal controls the average power delivered to the TE cell. As mentioned previously, to ensure rapid, well-defined behavior across various surfaces and skin types, a custom digital proportional–integral–derivative (PID) control scheme operates independently on each individual thermal stimulator. This control relies on a thermistor placed in proximity with the TE cell to record the temperature, digitized with the peripheral ADC. The CPU implements a numerical PID control with a 4 Hz refresh frequency to generate a PWM signal for each thermal stimulator. As a result, the PID control module drives the current demand from the TE cell, adjusting its value dynamically. For instance, immediately after activation for heating or cooling, the duty cycle on the PWM is close to 100% to overcome the thermal inertia from the ambient temperature. As the temperature approaches the set value, the PID adjusts the duty cycle to reach a balance between heat generation and loss, thus producing constant steady-state heat production and a corresponding fixed temperature. Fig. 3*D* illustrates a custom GUI with a 5 × 3 hybrid thermo-haptic unit array and 15 temperature readings in real time. The GUI allows users to freely adjust the thermo-haptic intensities and patterns. The operational lifetime based on the batteries used here depends largely on the level of dynamic interaction, typically between tens of minutes and a couple of hours.

Vibrotactile Perception Test of the Thermo-Haptic Stimulator. Sensory perception includes a coupling between mechanical and thermal stimulation because the four mechanoreceptors of vibration [P (Pacinian), NP I (Meissner), NP II (Ruffini), and NP III (Merkel cell-neurite)] have different working frequency ranges and thermal sensitivities. Pacinian corpuscles reach maximum sensitivity near the frequencies studied here (~100 Hz). With increasing temperature, the firing rate of this corpuscle increases and the reaction threshold decreases (38). Fig. 4*A* summarizes the results of two-point discrimination tests at different skin temperatures, conducted with pairs of thermo-haptic stimulators with set temperatures at 20, 30, and 40 °C for vibrations at frequencies of 100 Hz and amplitudes of 0.15 mm, with center-to-center separations of 12, 31, and 50 mm. At separations of 31 and 50 mm, the two vibrotactile stimuli can be distinguished at all three skin temperatures, as shown in Fig. 4*B*. A separation of 12 mm, however, the two stimuli can be distinguished only at 40 °C. Fig. 4*C* summarizes the increase in sensitivity to vibrations with increases in skin temperature. These effects influence the
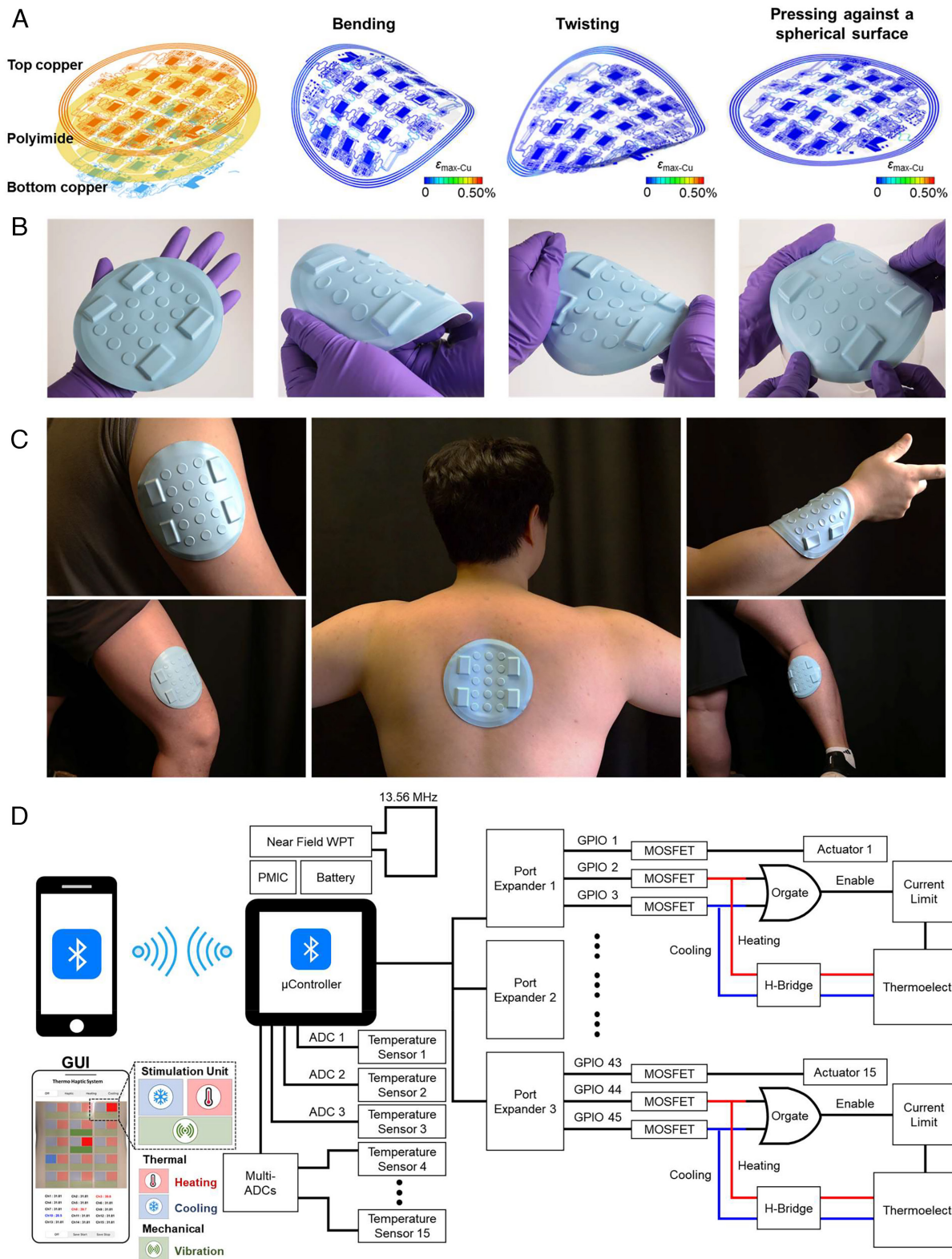
Fig. 3. Wireless, flexible, skin-integrated thermo-haptic system. (*A*) Finite-element modeling for cases of bending, twisting, and pressing against a spherical surface. The color represents the equivalent strain. (*B*) Photographs of the system in corresponding states of deformation. (*C*) Photographs of the system mounted on the upper arm, upper back, lower arm, upper leg, and lower leg. (*D*) Circuit, block diagram and connection mechanisms and wireless interface to a cellphone via Bluetooth communication. The illustration shows the graphical user interface (GUI) for thermal and vibrotactile stimulation. The *Inset* features a diagram that shows cooling (blue), heating (red), and vibration (green).

ability of a user to identify patterns of haptic actuation (left, up, down, and right, *SI Appendix*, Fig. S20), as demonstrated with participants using the system at temperatures set to 20, 30, and

40 °C (Fig. 4*D*). Each pattern involves vibrations at 100 Hz with amplitudes of 0.15 mm applied to three thermo-haptic stimulators located in these directions. Identification with the highest accuracy
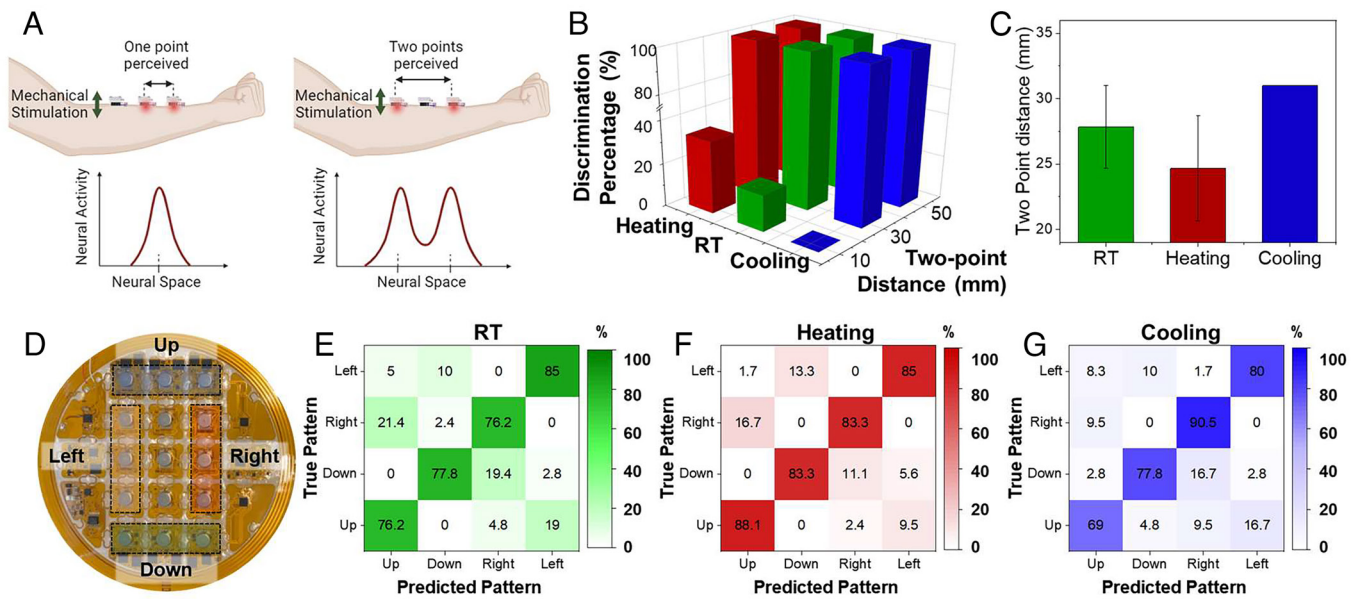
Fig. 4. Vibrotactile perception tests of thermo-haptic stimulators operating at different temperatures. (*A*) Schematic illustration of the two-point perception test conducted on the forearm. (*B*) Bar graph of two-point discrimination percentages at different temperatures (n = 6). (*C*) Bar graph of two-point discrimination distances at different temperatures (n = 6). (*D*) Schematic map of thermo-haptic stimulation patterns, *Up*, *Down*, *Left*, *Right* directions. Each pattern includes three stimulators. (*E–G*) Confusion matrix results of 30 blind perception tests for direction stimuli on the forearm using a combination of simultaneous mechanical and thermal stimulation at room (30 °C) (*E*), high (40 °C) (*F*), and low (20 °C) (*G*) temperatures (n = 6).

occurs at the highest temperature (Fig. 4 *E–G*), consistent with two-point discrimination tests.

Application Examples. The system introduced here can contribute significantly to tactile reconstruction by use of both temperature and tactile feedback, as illustrated in Fig. 5*A*. One example considers patients with impaired sensory function due to nerve damage. Other uses are in kinesthetic tactile learning and virtual training. The following describes control over robotic prosthetics and transfer of information from a mobile display, both of which integrate pressure and temperature sensors as control signals to operate the thermo-haptic stimulators via real-time wireless communication links.

The robotic hand used in these studies detects the temperature and pressure distributions associated with grasped objects through 15 thermistors cointegrated with a corresponding set of pressure sensors distributed across the fingers of the hand, as shown in Fig. 5*C* and *SI Appendix*, Fig. S21. The sensor data from the 15 locations of the robotic hand map in a one-to-one fashion to the thermo-haptic systems as shown in Fig. 5*D*. The temperature information passes directly as control signals to circuits that operate the TE cells; the pressure information passes indirectly to PWM settings for the ERM actuators, to define their amplitudes. Grasping a bottle filled with hot water with the robotic hand, as shown in the optical image and IR image of Fig. 5 *B* and *E* yields the pressure and temperature distributions shown in Fig. 5*F*. The measured pressures, across a range of 0 to 110 kPa convert to vibration intensities through control of the duty cycle of PWM, where 10%, 50%, and 100% correspond to pressures of 20, 60, and 80 kPa, respectively (Fig. 5 *G, i*). The thermal distribution reproduces directly, as shown in the IR image of Fig. 5 *G, iii* (Movie S2).

The second example involves a touch screen that includes a 5 × 3 array of transparent temperature sensors on a pressure-sensitive mobile device (iPhone X max, Apple) (Fig. 5*H*). Information captured in this manner passes to the thermo-haptic system following a scheme analogous to that for the robotic hand. Application of pressure with two fingers at different temperatures yields multi-touch information as shown in Fig. 5*I*. The pressure detected by

the touchscreen across a scale of 1 to 400 steps converts to a vibration intensity using the duty cycle of PWM, where 10%, 50%, and 100% correspond to pressures of 10, 20, and 30 kPa, respectively (Fig. 5 *J, i*). The different temperatures of the touched fingers appear on the thermo-haptic systems as shown in the IR image of Fig. 5 *J, ii* (Movie S3).

Discussion

The wireless, skin-integrated technology introduced here represents an advance in sensory augmentation that integrates arrays of thermo-haptic stimulators aligned with many engineering requirements for practical use. The vertical coupling scheme enables programmable patterns of enhanced vibrational displacement and dynamic thermal stimulation across large areas of the skin. The designs combine hard and soft materials into interfaces that offer skin-compatible mechanical compliance along with wirelessly programmable electronics, for high-resolution spatiotemporal thermo-haptic stimulation. The coupled mechanics of thermo-haptic stimulators lead to localized, intensified mechanical actuation. Combining miniaturized actuators with coupled interfaces will further improve the spatial resolution. Beyond its applications in reconstructing perception for prosthetic hands and touch displays described here, the closed-loop feedback systems, precise thermal control capabilities, and real-time user interfaces provide versatile options in sensory augmentation, with applications that span medicine, entertainment, and remote social interactions. Ongoing work aims to further reduce the sizes and weights of the stimulators and to expand the modes of mechanical stimulation beyond simple surface normal vibrations to include static displacements, shear deformations, and torsional motions.

Methods

Fabrication of the Thermo-Haptic Stimulator System. A flexible printed circuit board (fPCB;W153849ASS54, Xinyang) served as a substrate, with electrically defined circuit interconnects and soldering pads for the electronic
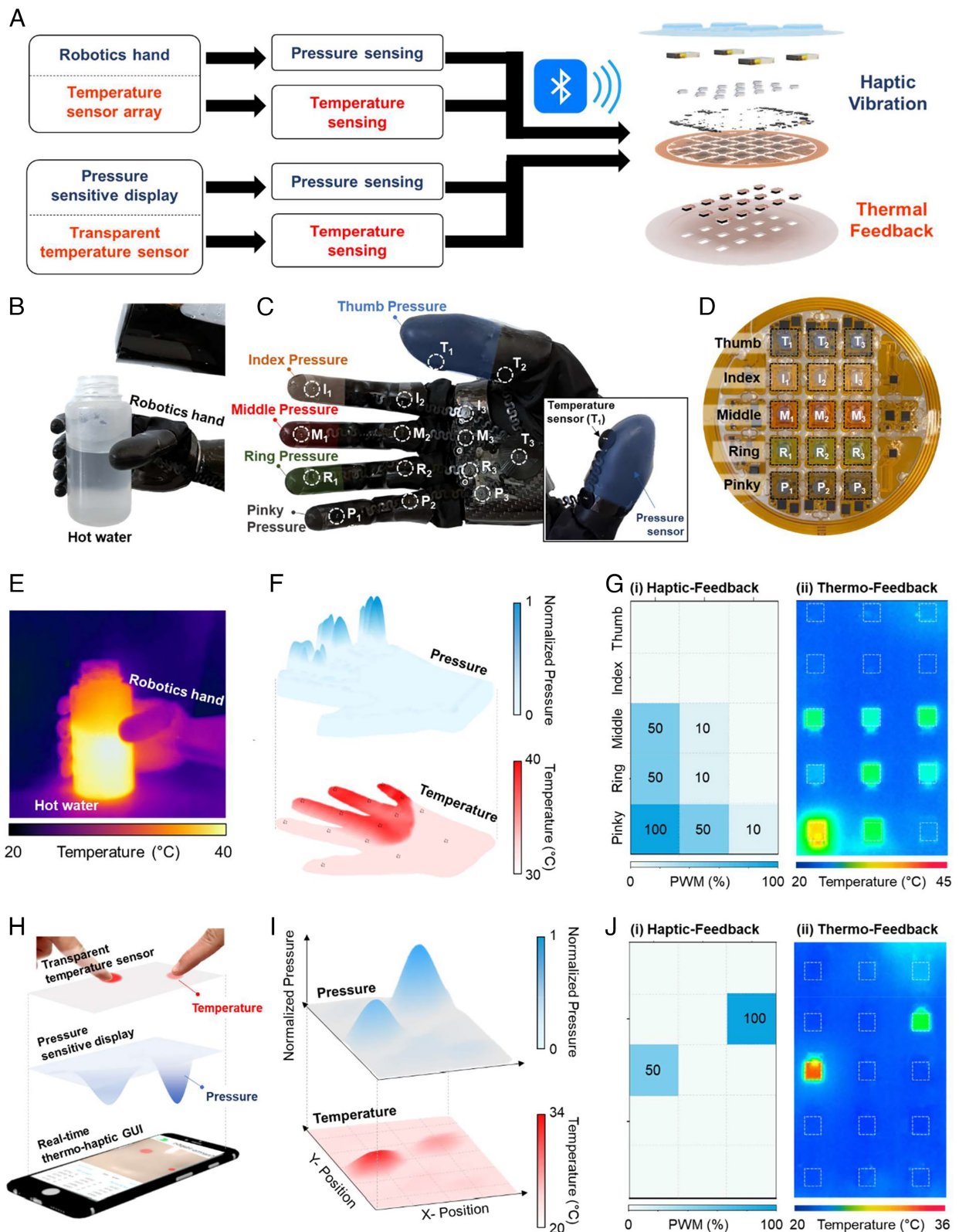
Fig. 5. Tactile reconstruction using the thermo-haptic system. (*A*) Flow chart of real-time measurements of distributions of pressure and temperature across a robotic hand and tactile display. (*B*) Photograph of the use of a robotic hand to grasp a bottle of hot water. (*C*) Photograph that highlights the locations of pressure and temperature sensors in the robotic hand. (*D*) Photograph and schematic map of thermo-haptic stimulators, where each stimulator corresponds to a position in the fingers of the robotic hand. (*E*) IR image of a robotic hand that grasps a hot bottle. (*F*) Measured distributions of pressure and temperature of a robotic hand while grasping a hot bottle. (*G*) Tactile reconstruction results of the robotic hand; (*i*) the distribution of PWM duty cycle and (*ii*) IR image of the thermo-haptic system for haptic and thermal feedback. (*H*) Exploded view schematic diagram of a tactile display with a transparent temperature sensor array. (*I*) Measured distribution of pressure and temperature across a multitouch tactile display. (*J*) Tactile reconstruction results of the tactile display; (*i*) the distribution of PWM duty cycle and (*ii*) IR image of the thermo-haptic system for haptic and thermal feedback.

components and stimulators. The fPCB consisted of a layer of polyimide (PI; 25 μm in thickness), patterned copper traces (Cu; 18 μm in thickness) on the top and bottom of surfaces, and polyimide encapsulation bonded by silicone adhesives (13 to 15 μm in thickness). Each notched island was joined by 700 μm wide serpentine interconnects with 500 μm wide Cu traces for current paths for the main power supply and electrical ground, along with two 200 μm wide Cu traces for other electrical connections. A Bluetooth system on chip (BLE SoC; CC2640R2FRSMT, Texas Instruments), multichannel analog-to-digital converters (m-ADCs; MAX11617EEE+T, Maxim Integrated), a port expander (XRA1201PIL24-F, MaxLinear), a full-bridge rectifier (BAS4002ARPPE6327HTSA1, Infineon Technologies), DC–DC converter (LM5166XDRCR, Texas Instruments), battery charger IC (STBC15QTR, STMicroelectronics), MOSFET H-bridge IC (DMHC10H170SFJ-13, Diodes Incorporated), current limiting IC (MIC2097-1YMT-TR, Microchip Technology), a 2-input OR gate (SN74LVC1G32QDRYRQ1, Texas Instruments), and essential passive components (resistors, capacitors, and inductors) electrically connect to pads on the fPCB through the use of a low temperature reflow process based on a lead free soldering paste (TS391LT, Chip Quik) activated with a hot air gun (AOYUE Int866). A collection of 15 ERM actuators (C0720B003D, Jinlong Machinery & Electronics) mount on Cu pads on the top side of the fPCB, and a corresponding set of 15 TE cells (430003-505, Laird Thermal Systems, Inc.) mount on Cu pads on the bottom side. The top and bottom Cu pads connect through 176 conductive holes to improve thermal conduction. A set of 15 FR-4 PCBs (W153849ASS45, Xinyang) with 15 thermistors (ERT-J0EV104F, Panasonic Electronic Components) were individually bonded next to the TE cells to measure the surface temperature of the skin at each corresponding location. A three-axis milling machine (Modela Pro II MDX 540, Roland DGA) produced molds in aluminum to define encapsulation layers. Specifically, a low-modulus silicone material (Silbione RTV 4420, Elkem) with a mixture of 10% white and 1% blue dyes (Silc Pig™, Smooth-On) served as the top encapsulating layer and a similar silicone material with 10% white dye served as the bottom layer. Molding involved compression and heating at 70 °C in an oven for 20 min. A custom die (20729, Millennium Die Group, Inc.) created openings in the bottom encapsulating layer aligned to the positions of the TE cells. Batteries (LP351221, Lipol Battery) reside inside of pouch structures in the top encapsulating layer, connected to pads of the fPCB with thin silicone encapsulated Cu wires (9564T1, McMaster-Carr). Placing uncured silicone material in between the two encapsulation layers clamped at followed by thermal curing at 70 °C in an oven for 30 min bonded the top and bottom. After cooling to the room temperature, a custom die (11111, Millennium Die Group, Inc.) defined the final interface shape by eliminating excessive encapsulating material at the edges.

Fabrication and Integration of Temperature Sensors into a Touch Screen and Robot Hand. The transparent temperature sensor array designed for integration into the touch screen application used 15 resistive temperature sensors, each with dimensions of 10.5×15 mm^2, and interconnects formed in a coating of Indium Tin Oxide (ITO) on a sheet of polyethylene terephthalate (PET, 639303, Sigma-Aldrich) patterned by laser ablation (ProtoLaser R4, LPKF Laser & Electronics). Each sensor mechanically and electrically connects to a corresponding pin of a board-to-board connector (527451633, Molex) soldered on top of a fPCB (W153849ASS48, Xinyang). The board-to-board connector served as an interface to the main electronic system of a BLE SoC, m-ADCs, and DC–DC converter using a serpentine structure to transmit temperature information from the touch screen via a BLE communication link. Similarly, a fPCB (W153849ASS54, Xinyang) mounted with a BLE SoC, m-ADCs, and DC–DC converter interfaces to temperature sensors placed at the positions of pressure sensors on the robotic prosthetic hand (Ability Hand, Psyonic, Inc.). Each temperature sensor includes interconnects in serpentine geometry to ensure robust operation during motions of the hand.

Experimental Apparatus for Measurements of Thermal Conductivity. Resistive heaters of two sizes (local: 4.5 mm diameter, global: 18 mm diameter) served as the basis for studies of changes in thermal conductivity of the skin under heat adaptation. Each heater resulted from laser ablation (ProtoLaser U4, LPKF Laser & Electronics) of an 18 μm thick layer of Cu on a fPCB (Pyralux AP8535R, DuPont). A digital multimeter (DMM; USB-4065; National Instruments), a commercial constant current source (2602 system Source Meter, Keithley Instruments), and an infrared camera (IR; FLIR Systems, a6255sc) enabled calibration of the heaters for different applied currents (10 to 60 mA, with an increment of 5 mA). LabVIEW (National

Instruments) software allowed automated adjustment of the current through the heater and measurements of the voltages at a sampling rate of 5 Hz.

Thermal conductivity measurements occurred under various conditions including different skin temperatures (32, 36, and 40 °C), residence times (1, 3, 5, and 10 min), and heater sizes (local: 4.5 mm diameter, global: 18 mm diameter). After each of the residence times, application of a small additional amount of heat (q) to the skin led to a corresponding change in temperature (ΔT_{skin}), as the basis for calculations of the thermal conductivity. Specifically, following previous work (29), the thermal conductivity of the skin can be calculated from the amount of heat transferred and the temperature change in the skin according to

$$\frac{\Delta T_{skin} k_{skin}}{qr} = f_1\left(\frac{\alpha_{skin} t}{r^2}\right) = 2\int_0^\infty \left\{ [J_1(x)]^2 \mathrm{erf}\left(\sqrt{\frac{\alpha_{skin} t}{r^2}}\right) \right\} \frac{dx}{x^2}, \quad [1]$$

where r is the radius of the heated area, q is the power per unit area, k_{skin} is the thermal conductivity of skin, α_{skin} is the thermal diffusivity of skin, t is the measurement time, J_1 is the Bessel function of the first kind, and erf is the error function. IR images captured the temperature distributions at the skin surface.

To account for thermal conductivity in operation of the thermal stimulator, the skin temperature time profile under contact with an arbitrary object was modeled by the following equation (34):

$$T_{skin}(t) = T_{skin,i} + \frac{B}{C}\left[1 - e^{\alpha_{skin} C^2 t}\mathrm{erfc}\left(C\sqrt{\alpha_{skin} t}\right)\right], \quad [2]$$

$$B = \frac{T_{obj,i} - T_{skin,i}}{k_{skin} R}, \quad [3]$$

$$C = \frac{1}{k_{skin} R}\left[1 + \frac{\sqrt{k_{skin} \rho_{skin} c_{skin}}}{\sqrt{k_{obj} \rho_{obj} c_{obj}}}\right], \quad [4]$$

where erfc is the complementary error function, T_{obj} is the temperature of an object, $T_{skin,i}$ and $T_{obj,i}$ are initial temperatures of the skin and object, t is the measurement time, k_{obj} is the thermal conductivity of the object, ρ_{skin} and ρ_{obj} are densities of the skin and object, c_{skin} and c_{obj} are the specific heat of the skin and object, and R is thermal contact resistance between the skin and object. These equations provide guidance for precise control of the magnitude and the rate of change in temperature to produce realistic sensations.

Finite-Element Analysis of the Stimulator System under Mechanical Loads. Three dimensional (3D) finite-element analysis (FEA) conducted with the commercial software Abaqus established essential aspects of the mechanical characteristics of the system during bending, twisting, stretching, and pressing against a spherical surface. The results defined the deformed configurations and strain/stress distributions under different levels of loading. The polyimide layers and the top and bottom copper traces were modeled with detailed geometric layouts using four-node shell elements. Polyimide was modeled as a linear elastic material with elastic modulus E_{PI} = 2.5 GPa and Poisson's ratio ν_{PI} = 0.34. Copper was modeled as elastoplastic (without hardening; yield strain chosen as 0.3%), with elastic modulus E_{Cu} = 119 GPa and Poisson's ratio ν_{Cu} = 0.34. For bending, the two opposite loading regions within the flexible PCB interface each rotated 60° (120° in total) to bend the system. For twisting, the two opposite loading regions within the fPCB each rotated 30° (60° in total). For stretching, displacements corresponding to 10% strain were applied to two opposite loading regions of the fPCB. For pressing against a spherical surface, four evenly spaced loading regions within the fPCB moved downward by 10 mm to contact a rigid spherical surface of 75 mm in radius.

Finite-Element Analysis of the Thermal Characteristics. Transient 3D heat transfer simulations performed in the commercial software COMSOL Multiphysics 6.0 allowed for quantitative studies of the temperature response of human skin to heating and cooling by the TE cell. One quarter of the stimulator system was modeled due to symmetry. Linear hexahedral elements were chosen to simulate both the skin and the TE cell. Experimentally measured values of the thermal conductivity of the human skin under different temperatures were input for simulation. The heat capacity and mass density of the human skin were chosen as 3,330 J kg^{-1} K^{-1} and 1,200 kg m^{-3} (39). Alumina (Al$_2$O$_3$) and bismuth telluride

(Bi_2Te_3) in the TE cell were modeled with thermal conductivity, heat capacity, and mass density of 30 W m^{-1} K^{-1}, 775 J kg^{-1} K^{-1}, and 3,900 kg m^{-3} for alumina (40), 1.6 W m^{-1} K^{-1}, 154.4 J kg^{-1} K^{-1}, and 7,740 kg m^{-3} (41) for bismuth telluride, and 16.3 W m^{-1} K^{-1}, 460 J kg^{-1} K^{-1}, and 7,817 kg m^{-3} (42, 43) for stainless steel. The copper (Cu) electrode sandwiched between Al_2O_3 and Bi_2Te_3 are thin (500 μm) and were thus neglected. To account for the Peltier effect, the heat flux $q = IT\Delta S$ was applied at the interface between Al_2O_3 and Bi_2Te_3. I is the operating current. T is the absolute temperature. ΔS is the difference between Seebeck coefficients of Bi_2Te_3 (200 μV/K) and Cu (6.5 μV/K) (41). The Peltier effect can describe the power–current relation (*SI Appendix*, Fig. S22) of the system (OptoTEC Series, Laird Thermal Systems GmBH). Joule heating also occurs in the Bi_2Te_3 region and its conductivity is 1.1×10^5 S/m. Heating involved a flux produced by the Peltier effect. Cooling involved a flux in the opposite direction. The external surface of the TE cell and skin can exchange heat with the environment at a temperature of 22 °C. The heat transfer coefficient was $h = 10$ W/(m^{2}K) (44).

PTV and 3D-DIC Experiments of the ERM Mechanics at Various Heights. PTV experiments for measuring oscillations of the ERM actuators as a function of h included recordings from a high-speed camera (2,048 × 1,088 in resolution; HT-2000 M, Emergent) with 35 mm imaging lenses (F1.4 manual focus; Kowa) at a sampling rate of 2,000 fps. The process tracked the center of the actuator center at 11 different values of h between 0 and 10 mm at 1 mm intervals, operating at 3 V on the phantom skin (16). A separate set of PTV experiments defined the effect of duty cycle, as shown in *SI Appendix*, Fig. S5A. Experiments involved operation of an ERM actuator at five different duty cycles ranging from 20 to 100% with 20% intervals at an input voltage of 3 V.

Three sets of 3D DIC experiments investigated deformations of the surrounding skin induced by an ERM actuator at h of 0, 3, and 6 mm. 3D displacements were captured by a pair of high-speed cameras (1,000 fps) used in the PTV experiments and processed using open-source 3D DIC software (MultiDIC) (24). The surrounding phantom skin was coated with black speckles by spray painting the surface. The DIC subset radius and spacing were s 20 and 10 pixels, respectively, resolving over 1,500 grids.

Modeling of the ERM Frequency and Amplitude. The ERM actuator mounted on the skin was modeled as a damped oscillator driven by an external force. The ordinary differential equation that describes the ERM system is

$$\frac{d^2x}{dt^2} + 2\Gamma\frac{dx}{dt} + \omega_0^2 x = a_0\sin(\omega t),\qquad [5]$$

where $\Gamma = \frac{\gamma}{2m}, \omega_0 = \sqrt{\frac{K}{m}}$, and $a_0 = \frac{F_0}{m}$, m is the mass of the eccentric mass, and ω is the angular velocity of the motor (angular frequency of the driving force), K is the effective stiffness of the ERM actuator, acrylic block, and skin layers, and γ is the damping coefficient of the skin. From the steady state solution of Eq. **5**, the amplitude of the actuator vibration (Amp) can be modeled as the following equation (45):

$$\text{Amp} = \frac{a_0}{\sqrt{\left(\omega_0^2 - \omega^2\right)^2 + 4\Gamma^2\omega^2}}.\qquad [6]$$

For the ERM system, the driving frequency is 942.47 rad/s < ω < 1,256.63 rad/s, or 150 Hz < f < 200 Hz, depending on the operating voltage. The stiffness of the acrylic block is defined as $K = \frac{EA}{h}$, where E is the Young Modulus, A is the area, and h is the height. Increasing h effectively lowers the stiffness and natural frequency ω_0 of the structure, consequently increasing the amplitude according to Eq. **6** as shown in Fig. 2*F* and *SI Appendix*, Fig. S2C.

The commercial software Abaqus determined the resonance frequency of the ERM using modal dynamics steps. The results defined the changes in resonant frequency for value of h between 1 and 10 mm, and skin modulus values E_1 between 100 and 500 kPa. A 3D space with dimensions of 100 mm × 100 mm × 20 mm (L × W × H) included a bilayer model of the skin with a top layer thickness of 2 mm to match the experimental phantom in *SI Appendix*, Fig. S4.

The displacement (U) and rotational (R) degrees of freedom were fixed for the element nodes at the skin. The total number of elements in the model was ~300,000. The elastic modulus (E), Poisson's ratio (υ), and density (ρ) used in the analytical model and FEA simulation were E_{skin} = 100 to 500 kPa, υ_{skin} = 0.49, and ρ_{skin} = 1,116 kg m^{-3} for the skin layers; E_{ERM} = 113 GPa and υ_{ERM} = 0.34, and ρ_{ERM} = 8,005 kg m^{-3} for the ERM motors; and $E_{acrylic}$ = 2.8 GPa and $\upsilon_{acrylic}$ = 0.37, and $\rho_{acrylic}$ = 1,180 kg m^{-3} for the acrylic blocks that set the values of h.

Data, Materials, and Software Availability. All study data are included in the article and/or supporting information.

Author affiliations: ^{a}Querrey-Simpson Institute for Bioelectronics, Northwestern University, Evanston, IL 60208; ^{b}Department of Electrical and Computer Engineering, University of Illinois at Urbana-Champaign, Urbana, IL 61801; ^{c}Department of Electrical and Computer Engineering, North Carolina State University, Raleigh, NC 27606; ^{d}Department of Mechanical and Aerospace Engineering, University of California San Diego, La Jolla, CA 92093; ^{e}Department of Mechanical Engineering, Pohang University of Science and Technology, Pohang 37673, Republic of Korea; ^{f}Department of Civil and Environmental Engineering, Northwestern University, Evanston, IL 60208; ^{g}Wearifi Inc., Evanston, IL 60208; ^{h}School of Electrical Engineering, Korea Advanced Institute of Science and Technology, Daejeon 34141, Republic of Korea; ^{i}Department of Mechanical Engineering, Rice University, Houston, TX 77005; ^{j}Department of Materials Science and Engineering, University of Illinois at Urbana Champaign, Urbana, IL 61801; ^{k}Department of Electronic Engineering, Hanyang University, Seoul 04763, Republic of Korea; ^{l}Department of Polymer Science and Engineering, Dankook University, Yongin 16890, Republic of Korea; ^{m}Department of Electrical and Computer Engineering, University of California, Davis, CA 95616; ^{n}Department of Electrical and Computer Engineering, Sungkyunkwan University, Suwon 16419, Republic of Korea; ^{o}Department of Mechanical Engineering, Northwestern University, Evanston, IL 60208; ^{p}Department of Semiconductor Convergence Engineering, Sungkyunkwan University, Suwon 16419, Republic of Korea; ^{q}Department of Biomedical Engineering, Northwestern University, Evanston, IL 60208; ^{r}Department of Materials Science and Engineering, Northwestern University, Evanston, IL 60208; and ^{s}Department of Neurological Surgery, Northwestern University, Chicago, IL 60208

Author contributions: J.-H.K., A.V.-G., J.-K.C., H.J., Y.H.J., J.-Y.Y., and J.A.R. designed research; J.-H.K., A.V.-G., H.L., J.-T.K., D.S.Y., H.Z., S.Y., C.P., Y.W., Z.C., S.K., R.A., J.U.K., Y.J.L., H.-S.S., M.Z., S.W.J., J.M.B., Y.L., S.Y.K., J.L., M.P., S.M.W., R.C., Y.H., Y.H.J., and J.-Y.Y. performed research; H.L., J.-T.K., R.A., Y.H., and J.-Y.Y. analyzed data; and J.-H.K., A.V.-G., J.-Y.Y., and J.A.R. wrote the paper.

1. M. J. Caterina *et al.*, The capsaicin receptor: A heat-activated ion channel in the pain pathway. *Nature* **389**, 816–824 (1997).
2. D. D. McKemy, W. M. Neuhausser, D. Julius, Identification of a cold receptor reveals a general role for TRP channels in thermosensation. *Nature* **416**, 52–58 (2002).
3. R. J. Schepers, M. Ringkamp, Thermoreceptors and thermosensitive afferents. *Neurosci. Biobehav. Rev.* **34**, 177–184 (2010).
4. R. M. Menorca, T. S. Fussell, J. C. Elfar, Peripheral nerve trauma: Mechanisms of injury and recovery. *Hand Clin.* **29**, 317–330 (2013).
5. R. M. Stassart *et al.*, A role for Schwann cell–derived neuregulin-1 in remyelination. *Nat. Neurosci.* **16**, 48–54 (2013).
6. R. W. Habash, R. Bansal, D. Krewski, H. T. Alhafid, Thermal therapy, part 1: An introduction to thermal therapy. *Crit. Rev. Biomed. Eng.* **34**, 459–489 (2006).
7. H. Jeong *et al.*, Closed-loop network of skin-interfaced wireless devices for quantifying vocal fatigue and providing user feedback. *Proc. Natl. Acad. Sci. U.S.A.* **120**, e2219394120 (2023).
8. C. A. Kubiak, T. A. Kung, D. L. Brown, P. S. Cederna, S. W. Kemp, State-of-the-art techniques in treating peripheral nerve injury. *Plast. Reconstr. Surg.* **141**, 702–710 (2018).
9. C. Pasluosta, P. Kiele, T. Stieglitz, Paradigms for restoration of somatosensory feedback via stimulation of the peripheral nervous system. *Clin. Neurophysiol. Pract.* **129**, 851–862 (2018).
10. P. Svensson, U. Wijk, A. Björkman, C. Antfolk, A review of invasive and non-invasive sensory feedback in upper limb prostheses. *Expert. Rev. Med. Devices* **14**, 439–447 (2017).
11. M. P. Willand, M.-A. Nguyen, G. H. Borschel, T. Gordon, Electrical stimulation to promote peripheral nerve regeneration. *Neurorehabil. Neural. Repair.* **30**, 490–496 (2016).
12. Y. Huang *et al.*, A skin-integrated multimodal haptic interface for immersive tactile feedback. *Nat. Electron.* **6**, 1020–1031 (2023).
13. Y. H. Jung, J. H. Kim, J. A. Rogers, Skin-integrated vibrohaptic interfaces for virtual and augmented reality. *Adv. Funct. Mater.* **31**, 2008805 (2021).
14. X. Yu *et al.*, Skin-integrated wireless haptic interfaces for virtual and augmented reality. *Nature* **575**, 473–479 (2019).
15. M. Zhu *et al.*, Haptic-feedback smart glove as a creative human-machine interface (HMI) for virtual/augmented reality applications. *Sci. Adv.* **6**, eaaz8693 (2020).
16. J.-T. Kim *et al.*, Mechanics of vibrotactile sensors for applications in skin-interfaced haptic systems. *Extreme Mech. Lett.* **58**, 101940 (2023).
17. W. Lin *et al.*, Super-resolution wearable electrotactile rendering system. *Sci. Adv.* **8**, eabp8738 (2022).
18. M. Ying *et al.*, Silicon nanomembranes for fingertip electronics. *Nanotechnology* **23**, 344004 (2012).
19. Y. Zhou *et al.*, A multimodal magnetoelastic artificial skin for underwater haptic sensing. *Sci. Adv.* **10**, eadj8567 (2024).
20. Y. H. Jung *et al.*, A wireless haptic interface for programmable patterns of touch across large areas of the skin. *Nat. Electron.* **5**, 374–385 (2022).
21. S. Hong *et al.*, Wearable thermoelectrics for personalized thermoregulation. *Sci. Adv.* **5**, eaaw0536 (2019).

22. R. A. Kishore, A. Nozariasbmarz, B. Poudel, M. Sanghadasa, S. Priya, Ultra-high performance wearable thermoelectric coolers with less materials. *Nat. Commun.* **10**, 1765 (2019).
23. M. Park *et al.*, Skin-integrated systems for power efficient, programmable thermal sensations across large body areas. *Proc. Natl. Acad. Sci. U.S.A.* **120**, e2217828120 (2023).
24. D. Solav, K. M. Moerman, A. M. Jaeger, K. Genovese, H. M. Herr, MultiDIC: An open-source toolbox for multi-view 3D digital image correlation. *IEEE Access* **6**, 30520–30535 (2018).
25. R. W. Cholewiak, J. C. Brill, A. Schwab, Vibrotactile localization on the abdomen: Effects of place and space. *Percept. Psychophys.* **66**, 970–987 (2004).
26. K. O. Johnson, The roles and functions of cutaneous mechanoreceptors. *Curr. Opin. Neurobiol.* **11**, 455–461 (2001).
27. J.-T. Kim, L. P. Chamorro, Coupled mechanics in skin-interfaced electronics via computer vision methods. *Soft. Sci.* **4**, 12 (2024).
28. D. R. Kenshalo, C. E. Holmes, P. B. Wood, Warm and cool thresholds as a function of rate of stimulus temperature change. *Percept. Psychophy.* **3**, 81–84 (1968).
29. D. Filingeri, H. Zhang, E. A. Arens, Characteristics of the local cutaneous sensory thermoneutral zone. *J. Neurophysiol.* **117**, 1797–1806 (2017).
30. I. Ezquerra-Romano, A. Ezquerra, Highway to thermosensation: A traced review, from the proteins to the brain. *Rev. Neurosci.* **28**, 45–57 (2017).
31. S. R. Madhvapathy *et al.*, Epidermal electronic systems for measuring the thermal properties of human skin at depths of up to several millimeters. *Adv. Funct. Mater.* **28**, 1802083 (2018).
32. J. M. Johnson, D. L. Kellogg Jr., Local thermal control of the human cutaneous circulation. *J. Appl. Physiol.* **109**, 1229–1238 (2010).
33. D. L. Kellogg Jr., In vivo mechanisms of cutaneous vasodilation and vasoconstriction in humans during thermoregulatory challenges. *J. Appl. Physiol.* **100**, 1709–1718 (2006).
34. L. A. Jones, H.-N. Ho, Warm or cool, large or small? The challenge of thermal displays. *IEEE Trans. Haptics.* **1**, 53–70 (2008).
35. Y. Chen, J. Ma, W. Li, Understanding the thermal conductivity and Lorenz number in tungsten from first principles. *Phys. Rev. B.* **99**, 020305 (2019).
36. T. Reddyhoff, A. Schmidt, H. Spikes, Thermal conductivity and flash temperature. *Tribol. Lett.* **67**, 1–9 (2019).
37. C. Stabler *et al.*, Thermal properties of SiOC glasses and glass ceramics at elevated temperatures. *Materials* **11**, 279 (2018).
38. R. T. Verrillo, S. J. Bolanowski, Effects of temperature on the subjective magnitude of vibration. *Somatosens. Mot. Res.* **20**, 133–137 (2003).
39. M. Fu, W. Weng, H. Yuan, Numerical simulation of the effects of blood perfusion, water diffusion, and vaporization on the skin temperature and burn injuries. *Num. Heat. Transf. A. Appl.* **65**, 1187–1203 (2014).
40. P. Auerkari, *Mechanical and Physical Properties of Engineering Alumina Ceramics* (Technical Research Centre of Finland Espoo, 1996).
41. E. E. Antonova, D. C. Looman, "Finite elements for thermoelectric device analysis in ANSYS" in *Proceedings of ICT 2005. 24th International Conference on Thermoelectrics*, T. Tritt. Ed. (IEEE, Clemson, SC, 2005), pp. 215–218.
42. L. Liang, Y. Quan, Z. Ke, Investigation of tool-chip interface temperature in dry turning assisted by heat pipe cooling. *Int. J. Adv. Manuf. Technol.* **54**, 35–43 (2011).
43. N. Atabaki, B. Baliga, Effective thermal conductivity of water-saturated sintered powder-metal plates. *Heat. Mass. Transf.* **44**, 85–99 (2007).
44. Y. Zhang *et al.*, Theoretical and experimental studies of epidermal heat flux sensors for measurements of core body temperature. *Adv. Healthc. Mater.* **5**, 119–127 (2016).
45. J. B. Marion, *Classical Dynamics of Particles and Systems* (Academic Press, 2013).